

pubs.acs.org/JPCA Article

Influence of Aliphatic versus Aromatic Ligand Passivation on Intersystem Crossing in $Au_{25}(SR)_{18}^-$

Nathanael L. Smith and Kenneth L. Knappenberger, Jr.*



Cite This: J. Phys. Chem. A 2024, 128, 7620-7627



Read Online

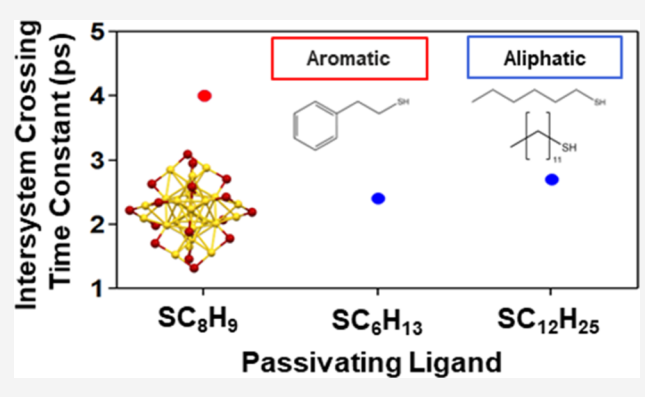
ACCESS I

III Metrics & More

Article Recommendations

s Supporting Information

ABSTRACT: The electronic relaxation dynamics of gold monolayer protected clusters (MPCs) are influenced by the hydrocarbon structure of thiolate protecting ligands. Here, we present ligand-dependent electronic relaxation for a series of $\mathrm{Au}_{25}(\mathrm{SR})_{18}^-$ (SR = $\mathrm{SC}_8\mathrm{H}_9$, $\mathrm{SC}_6\mathrm{H}_{13}$, $\mathrm{SC}_{12}\mathrm{H}_{25}$) MPCs using femtosecond time-resolved transient absorption spectroscopy. Relaxation pathways included a ligand-independent femtosecond internal conversion and a competing ligand-dependent picosecond intersystem crossing process. Intersystem crossing was accelerated for the aliphatic ($\mathrm{SC}_6\mathrm{H}_{13}$, $\mathrm{SC}_{12}\mathrm{H}_{25}$) thiolate MPCs compared to the aromatic ($\mathrm{SC}_8\mathrm{H}_9$) thiolate MPCs. Additionally, a 1.2 THz quadrupolar acoustic mode and a 2.4 THz breathing acoustic mode was identified in each cluster, which indicated that differences in ligand structure did not



result in significant structural changes to the metal core of the MPCs. Considering that the difference in relaxation rates did not result from ligand-induced core deformation, the accelerated intersystem crossing was attributed to greater electron-vibrational coupling to Au–S vibrational modes. The results suggested that the organometallic semiring was less rigid for the aliphatic thiolate MPCs due to reduced steric effects, and in turn, increases in nonradiative decay rates were observed. Overall, these results imply that the protecting ligand structure can be used to modify carrier relaxation in MPCs.

INTRODUCTION

The optical, electronic, mechanical, and magnetic properties of noble metal nanoparticles are determined by nanoparticle structure. 1-9 An important component of the nanoparticle structural framework is the passivating ligand. Beyond providing solution stability, the ligand affects electronic coherence, electron-vibrational coupling, and electronic relaxation pathways. 10-13 Consequently, the ligand can act as a chemical handle to guide carrier relaxation. Monolayer protected clusters (MPCs) are a class of structurally precise colloidal nanoparticles with a well-defined metal-ligand interface. Thiolate MPCs consist of 3 structural domains: (i) an all-metal atom core, surrounded by (ii) an organometallic semiring that anchors (iii) the protecting, typically hydrocarbon, ligands. In many instances, the protecting ligand can be exchanged with minimal or no disturbance to the structure as a whole. 14 In other instances, ligand exchange can be used to drive structural rearrangement of the MPC. 15 Thus, MPCs offer a tailorable platform to investigate how ligand structure affects electronic relaxation in metal nanoparticles.

MPCs offer unique interfacial structural control compared to larger nanoparticles. ¹⁶ In MPCs, the metal—ligand interface is atomically well-defined, and it can be tailored through the protecting ligand. The size, structure, and electronic relaxation dynamics of the MPC can be controlled or modified by the choice of the protecting ligand. ^{17,18} For larger plasmonic

nanoclusters, the ligand -R group changes the plasmon dephasing time and the strength of electron-vibrational coupling. ¹⁹ In smaller MPCs, where single electron transitions occur between quantized electronic states, the ligand structure can be expected to influence nonradiative relaxation pathways through modulation of the electron-vibrational coupling strength.

 ${\rm Au_{25}(SR)_{18}}^-$ is a modular MPC making it suitable for isolating the effects of ligand structure on carrier relaxation. It consists of a 13 Au atom icosahedral core surrounded by 6 ${\rm Au_2SR_3}$ staple units in a pseudo-octahedral geometry. Common modifications include doping the core or semiring with metal atoms, exchanging the anchoring atom in the semiring, and substituting the organic functional groups in the ligand. $^{20-22}$ In each case, these modifications can be made without disturbing the structural framework. In particular, ${\rm Au_{25}(SR)_{18}}^-$ can be directly synthesized with various protecting ligands. The solved structures from single-crystal

Received: July 1, 2024
Revised: August 15, 2024
Accepted: August 19, 2024
Published: August 28, 2024





X-ray diffraction confirm that substitution from an aromatic (SC_8H_9) to an aliphatic $(SC_2H_5, SC_3H_7, SC_4H_8)$ ligand preserves the $Au_{25}(SR)_{18}^-$ core geometry and staple unit arrangement. ^{23–25} Generally, the Au–Au bond lengths of the icosahedral core and the Au-S bond lengths are identical, while the distance separating Au atoms of the core and staple units is increased for the aliphatic series. Furthermore, electronic states are strongly coupled to Au-S vibrational modes and Au-S vibrational modes mediate relaxation between excited states in $\mathrm{Au}_{25}(\mathrm{SR})_{18}^{-26-28}$ Inter- and intraligand interactions modify Au-S vibrational spectra.²⁹ In particular, pronounced Au-S torsional modes are measured for phenylethanethiol substituted Au₂₅(SR)₁₈-, whereas these signals are more diffuse when alkanethiols are used. 30,31 Consequently, ligand structure can be expected to influence vibrationally mediated excited carrier relaxation. Therefore, Au₂₅(SR)₁₈⁻ is an optimal system to interrogate the effects of hydrocarbon ligand structure on electronic relaxation rates and pathways in nanoparticles.

The influence of aromatic and aliphatic hydrocarbon ligand structure on the electronic relaxation dynamics of Au₂₅(SR)₁₈ was investigated using femtosecond transient absorption. Three $Au_{25}(SR)_{18}$ MPCs were synthesized with SC_8H_{9} SC_6H_{13} , and $SC_{12}H_{25}$ as protecting ligands. Identical frequency modulation of the transient absorption signal by acoustic phonon modes indicated that the Au core was not deformed by the ligands. The MPCs displayed ligand-dependent picosecond relaxation dynamics which were assigned to intersystem crossing. The intersystem crossing rate was slowed for the aromatic MPC compared to the aliphatic MPCs. This effect was attributed to a rigidified semiring due to steric interactions and the π bonding network between the aromatic ligands. As a result, Au-S mediated electronic relaxation was slowed due to reduced electronic-vibrational coupling for clusters with aromatic ligand substituents. A more flexible semiring in the aliphatic MPCs accelerated intersystem crossing and resulted in increased branching ratios for this carrier relaxation pathway.

METHODS

Synthesis of Au₂₅(SR)₁₈⁻. Au₂₅(SR)₁₈⁻ was synthesized according to literature. A flask was charged with HAuCl₄· $3H_2O$ (400 mg, 1.01 mmol) and TOAB (200 mg, 1.14 mmol). The reagents were dissolved in 28 mL of THF under constant stirring. After 15 min, either phenylethanethiol, hexanethiol, or dodecanethiol (5.36 mmol) was added. The solution was left to stir for 12 h, after which NaBH₄ (386 mg, 10 mmol) dissolved in 10 mL of ice-cold water was added rapidly. The solution was left to stir for 48 h.

The solution was gravity filtered to remove insoluble materials. The THF layer was evaporated and the product was redissolved into toluene. Next, the solution was extracted with water and the toluene layer was collected. The solvent was evaporated and the product was washed with methanol. The cluster was dissolved off the frit with DCM and then dried to yield $[TOA^+][Au_{25}(SR)_{18}^-]$.

UV-Vis Spectroscopy. UV-visible extinction spectra were acquired with an Aligent Cary 60 spectrophotometer, using a quartz cuvette with a 1 cm path length and a background scan of DCM.

Femtosecond Transient Absorption Spectroscopy. Transient absorption spectroscopy was carried out on a system previously described.³³ The 1040 nm fundamental from a 100

kHz ytterbium amplifier seeded a noncollinear optical parametric amplifier (NOPA) (Spectra-Physics Spirit-NOPA) to generate visible pulses for the pump. A portion of the fundamental was passed through a 1 cm thick sapphire crystal to generate the continuum probe pulse that extended from 540 to 840 nm. The white light was collimated and compressed with chirped mirrors. The pump and probe beams were focused on the sample by a parabolic mirror where temporal and spatial overlap was achieved. The temporal instrument response, determined by the nonresonant solvent response, was 93 fs in duration. Pump pulse energies at the sample were 8 nJ.

■ RESULTS AND DISCUSSION

Frequency Domain Analysis. The normalized linear absorption spectrum for each MPC is presented in Figure 1a.

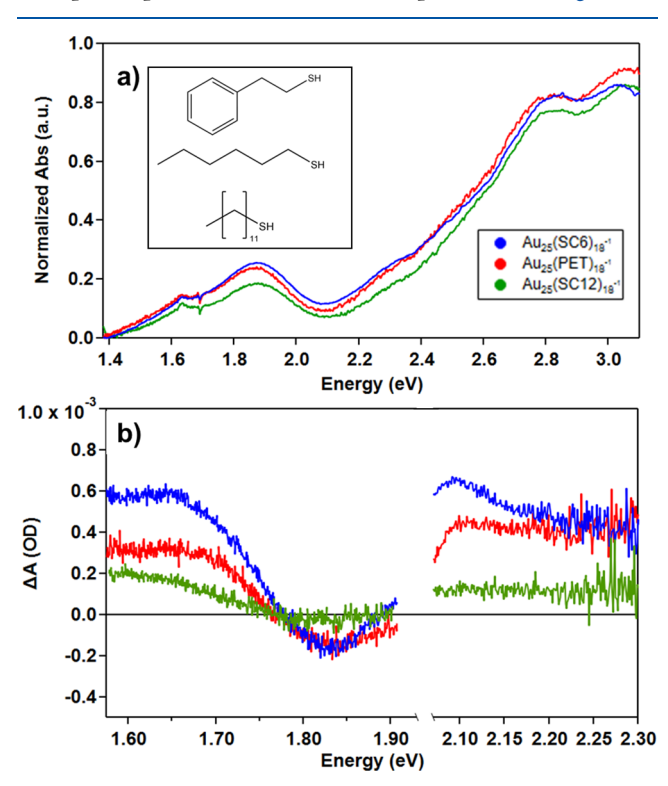


Figure 1. (a) UV—vis absorption spectra for the MPCs are qualitatively similar. The ligand has no resolvable effect on the low energy (1.6—2.0 eV) core-based transitions. Higher energy transitions originate from semiring electronic states and exhibit no significant changes upon ligand exchange. (b) Transient spectra acquired at 1 ps pump—probe delay time after core localized excitation at 2.0 eV. The 1.85 eV transition is bleached for each cluster. Differences in the excited state absorption peaks at higher energy probe are a result of the passivating ligands. The transient spectra have been plotted with a break in the energy axis to exclude pump scatter.

The MPCs of interest were $\mathrm{Au}_{25}(\mathrm{SC}_8\mathrm{H}_9)_{18}^-$, $\mathrm{Au}_{25}(\mathrm{SC}_6\mathrm{H}_{13})_{18}^-$, and $\mathrm{Au}_{25}(\mathrm{SC}_{12}\mathrm{H}_{25})^-$, where $(\mathrm{SC}_8\mathrm{H}_9)$, $(\mathrm{SC}_6\mathrm{H}_{13})$, and $(\mathrm{SC}_{12}\mathrm{H}_{25})$ are the aromatic phenylethanethiol and aliphatic hexanethiol and dodecanethiol ligands, respectively. The inset of Figure 1 depicts the protecting ligand structure. For the following discussions, these clusters are abbreviated as $\mathrm{Au}_{25}(\mathrm{PET})_{18}^-$, $\mathrm{Au}_{25}(\mathrm{SC6})_{18}^-$ and $\mathrm{Au}_{25}(\mathrm{SC12})_{18}^-$.

The absorption spectra for each of the three clusters are qualitatively similar. Two peaks are present at 1.6 and 1.8 eV which correspond to superatomic intraband LUMO \leftarrow

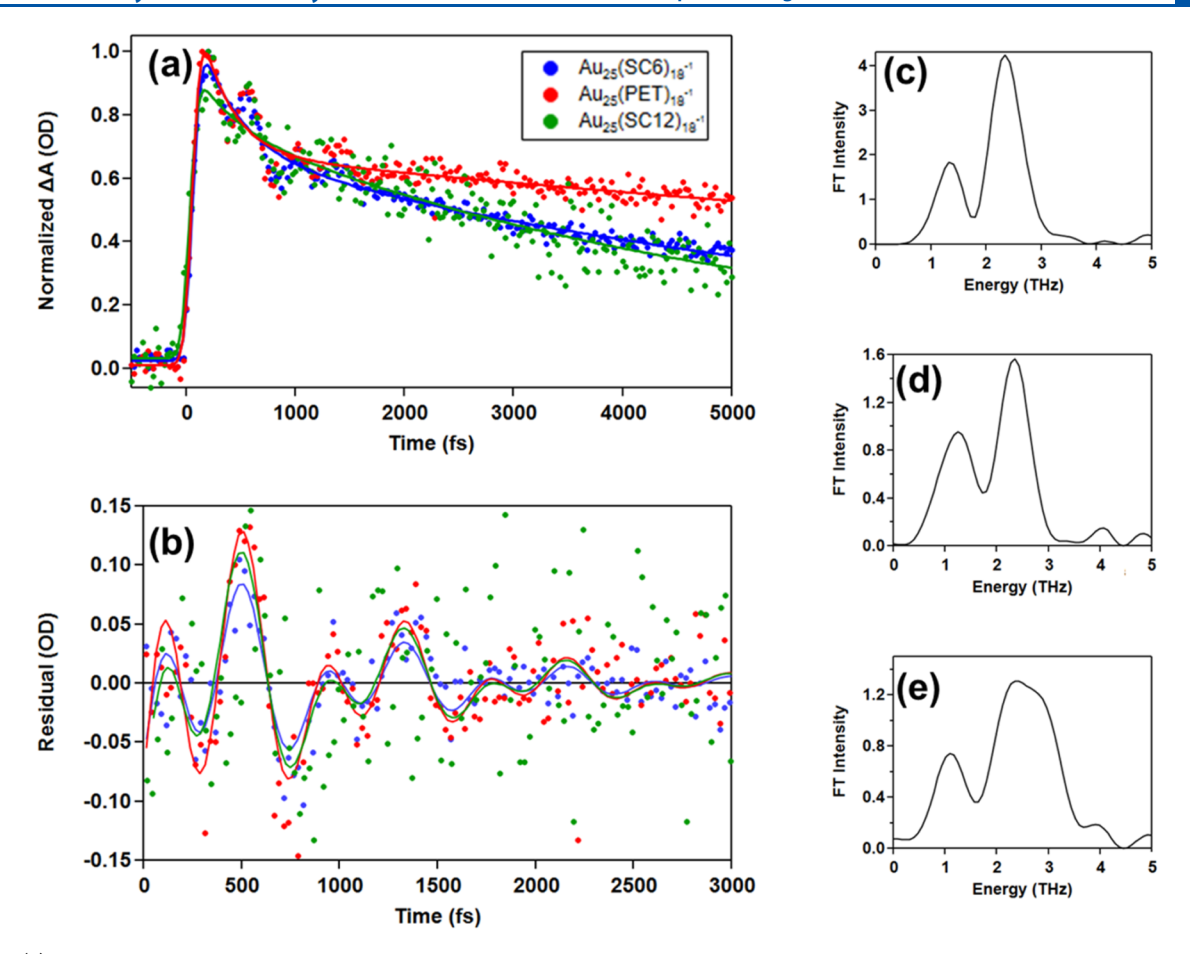


Figure 2. (a) Kinetic traces extracted at 1.60 eV probe energy, fitted to a sum of three exponentials. Coherent oscillations modulate the signal at early time delays. (b) The isolated coherent residuals are nearly identical in phase, amplitude, and frequency when fit to a sum of two damped harmonic oscillators. The Fourier spectra of the coherent residuals from panel (b) for (c) $Au_{25}(PET)_{18}^{-}$, (d) $Au_{25}(SC6)_{18}^{-}$, and (e) $Au_{25}(SC12)_{18}^{-}$ yield identical frequencies of 1.2 THz and 2.4 THz for each MPC.

HOMO and LUMO \leftarrow HOMO - 1 transitions, respectively. Density functional theory (DFT) calculations characterize the HOMO and HOMO - 1 as superatomic p orbitals and the LUMO as superatomic d orbitals. Degeneracies in the p orbital manifold and d orbital manifold are lifted due to MPC symmetry and spin—orbit coupling. The energy of core transitions can change due to electron delocalization by the protecting ligand that expands the Au core. Signary For these hydrocarbon thiolate ligands, the choice of ligand does not affect the core transitions energies (Figure 1a). At higher energies, transitions originate from the ligand band, with ligand contributions increasing as excitation energy also increases. Each MPC features peaks near 2.7 and 3.1 eV. Overall, the ligand choice does not result in a resolvable difference in the excitation energy of the Au intraband or interband transitions.

Transient absorption measurements for all three clusters were performed at 2.0 eV excitation, which was resonant with LUMO \leftarrow HOMO manifold transitions. Figure 1b portrays the transient spectrum at 1 ps pump—probe time delay for each MPC. Three distinct regions were apparent: (1) low-energy excited state absorption spanning 1.65–1.75 eV, (2) a transient bleach centered at 1.85 eV, and (3) high-energy excited state absorption for probe energies exceeding 2.0 eV. As was the case for steady-state linear absorption spectroscopy, the transient spectral features were similar across the three clusters.

Coherent Time-Domain Analysis. The coherent oscillations in the time-domain data were analyzed first to evaluate if the protecting ligand induced structural changes within the $\mathrm{Au}_{25}(\mathrm{SR})_{18}^-$ series. Figure 2a displays the overlaid kinetic traces taken at 1.60 eV probe and truncated to 5 ps. The incoherent population decay was modeled as a sum of three exponentials convoluted with the Gaussian instrument response

$$\Delta A = a_0 + \sum_i \frac{a_i}{t_i} \times \exp \text{gauss}\left(\frac{t}{t_i}\right)$$
 (1)

where a_0 represents the DC offset, a_i is the amplitude of ith component, t_i is the time constant of ith component and expgauss represents an exponential convoluted with a Gaussian. The best fits are described as a ligand-independent femtosecond decay, a ligand-dependent picosecond decay, and a long-lived decay outside the temporal range of this experiment. The full dynamics and ligand dependence of the incoherent electronic relaxation are discussed later ($vide\ infra$).

At early time delays (<3 ps), the transient absorption signal is modulated by low-frequency amplitude oscillations. Coherent acoustic modes are launched upon ultrafast excitation of the MPC, resulting in mechanical vibrations of the clusters that exhibit periodic modulations to the time-domain signal. The coherent transient signal was isolated by subtracting the incoherent electronic relaxation fits, as

modeled by eq 1, from the time-domain traces. Figure 2b overlays the obtained coherent residuals, corrected for time zero. Fit lines for the coherent oscillations were obtained by modeling the residual as a sum of two damped harmonic oscillators

$$Res = \sum_{i} A_{i} \times \exp\left(-\frac{t}{t_{1i}}\right) \sin\left(\frac{2\pi}{t_{2i}} + \varphi_{i}\right)$$
(2)

where A_i is the amplitude of ith component, t_{1i} is the dephasing lifetime, t_{2i} is the period, and φ_i is the initial phase. The coherent residuals of the three MPCs are nearly identical in frequency, phase, and amplitude. The fit frequencies were obtained from the Fourier transform of the time domain residuals to the frequency domain data. The resultant Fourier spectra are shown in Figure 2c-e, for clusters $\text{Au}_{25}(\text{PET})_{18}^-$, $\text{Au}_{25}(\text{SC6})_{18}^-$, and $\text{Au}_{25}(\text{SC12})_{18}^-$, respectively. For $\text{Au}_{25}(\text{PET})_{18}^-$ the retrieved frequencies were 1.3 ± 0.5 THz and 2.4 ± 0.4 THz, for $\text{Au}_{25}(\text{SC6})_{18}^ 1.2 \pm 0.8$ THz and 2.3 ± 0.6 THz, and for $\text{Au}_{25}(\text{SC12})_{18}^ 1.1 \pm 0.6$ THz and 2.5 ± 1.6 THz. The error represents the full width at half-maximum from the Gaussian fit of the peak. Within error, the coherent residuals of the three MPCs are identical in frequency.

Two acoustic modes modulate the time-dependent signal: a symmetric expansion and contraction of the Au atoms known as the breathing mode, and a higher order quadrupolar dilation-compression of the inorganic unit.^{39,40} The elastic frequency law describes the size dependence of the acoustic modes. The quadrupolar mode frequency scales with the radius of the MPC (1/R). For $Au_{25}(SR)_{18}^{-}$, the quadrupolar mode is predicted to be near 1.2 THz. Theory predicts that the breathing mode does not follow the elastic frequency law and is independent of MPC size.⁴¹ Experimentally, the breathing mode has been found to be near 2.4 THz. 6,37,38,42,43 As a result, we assign the low frequency oscillation as the quadrupolar mode and the high frequency oscillation as the breathing mode. Further support of these assignments is seen in the frequency modulation of the bleach peak position, which oscillated with a frequency of 2.4 THz (Figures S1 and S2). Additionally, the coherent residual of the high-energy excited state absorption (ESA) was modulated by a 1.2 THz frequency mode (Figure S3). Because the 1.2 THz and 2.4 THz oscillations are independently present at other probe wavelengths, these are two fundamental acoustic modes and not a fundamental mode and its harmonic overtone.

Given that the mechanical modes are sensitive to overall structure, the acoustic mode frequencies can be used as a probe for distortion of the Au core. In particular, the quadrupolar mode is sensitive to the size and shape of the Au core. The quadrupolar mode frequency scales linearly with MPC radius for spherical core geometries. In the case of core elongation, the quadrupolar mode degeneracy is broken and a lower frequency extensional mode dominates.³⁹ For the rodlike Au₂₅ MPC, the quadrupolar mode decreases in frequency to 0.8 THz. 44 Additionally, geometric changes to the Au core can affect the amplitude and dephasing time of the coherent oscillations. The structural isomers of Au₃₈(PET)₂₄ present isomer-unique oscillation amplitudes and dephasing times.⁴⁵ Based on the agreement in frequency, amplitude, and quality factor of the quadrupolar coherent oscillations for all three nanoclusters, it is concluded that the Au₂₅(SR)₁₈ core structure was retained upon ligand substitution. This result was consistent with the crystal structures determined for

 ${\rm Au_{25}(PET)_{18}}^-$ and ${\rm Au_{25}(SC_3H_9)_{18}}^-$ which show that the inorganic structural framework remains unchanged for both the aliphatic and aromatic thiolate MPC. Thus, differences in the electronic relaxation should occur from structural changes within the ligand shell and semiring and not from structural distortion of the Au core.

The breathing mode frequency was also analyzed for the MPC series. In principle, the breathing mode frequency should be sensitive to mass loading effects from the protecting ligands. Although there are mass differences between the ligands, the expected shifts in frequency would fall within the two standard deviations of the retrieved Fourier frequencies. We conclude that our measurements would not be sensitive to these changes. Previous transient absorption measurements on $\mathrm{Au}_{25}(\mathrm{SR})_{18}^{-}$ detected no dependence of the breathing mode frequency on the protecting ligand.

Incoherent Time-Domain Analysis. To understand the influence of the protecting ligand on electronic relaxation, the picosecond time scale dynamics were analyzed. Figure 3a

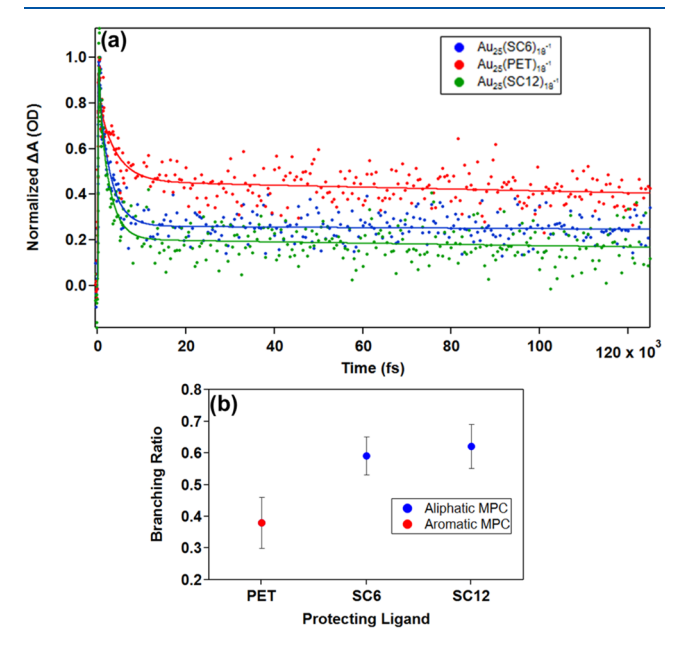


Figure 3. Kinetic traces acquired at 1.60 eV probe energy extending to 120 ps pump—probe delay time. The solid lines represent the fitting kinetics, which are as described: a ~ 300 fs internal conversion, a ligand-dependent picosecond intersystem crossing, and a long-time radiative and nonradiative. Intersystem crossing is accelerated for the MPCs protected with aliphatic ligands compared to the MPCs with aromatic ligands. The bulky aromatic ligands restrict vibrational motion of the organometallic semiring (Au–S stretch) and decreases electron-vibrational coupling, which in turn, reduces the efficiency (i.e., decelerates) ISC.

displays the full-length kinetic traces extracted at 1.60 eV probe along with lines that represent the fit results. The incoherent population decay is described by a rapid ligand-independent 300 fs decay, a ligand-dependent picosecond decay, and a long-lived decay that persisted beyond the temporal acquisition range of the experiment. The picosecond decay time constant was 4 ps for $\mathrm{Au}_{25}(\mathrm{PET})_{18}^-$. In the aliphatic thiolate-protected MPCs the picosecond decay was accelerated. The decay time constants are 2.7 and 2.4 ps for $\mathrm{Au}_{25}(\mathrm{SC6})_{18}^-$ and $\mathrm{Au}_{25}(\mathrm{SC12})_{18}^-$, respectively, reflecting an approximate 1.5x acceleration of the decay rate constant for aliphatic substituted

nanoclusters. Additionally, the amplitude constant of the picosecond decay component was much greater for the aliphatic MPCs. Figure 3b presents the ligand-dependent branching ratios of the picosecond decay amplitude constant to the sum of all amplitude coefficients for the fit.

Internal conversion between core electronic states occurs on the femtosecond time scale. Rapid internal conversion to the highest occupied molecular orbital—lowest unoccupied molecular orbital (HOMO–LUMO) manifold within 100s of femtoseconds is characteristic to MPCs. 43,47 For $\mathrm{Au}_{25}(\mathrm{PET})_{18}^-$, $\mathrm{Au}_{25}(\mathrm{SC6})_{18}^-$, and $\mathrm{Au}_{25}(\mathrm{SC12})_{18}^-$ the best-fit decay time constants were 300, 400, and 300 fs, respectively. Defining the error as the 93 fs instrument response, each of these processes were within error of one another. These time constants are consistent with two-dimensional electronic spectroscopy measurements on $\mathrm{Au}_{25}(\mathrm{PET})_{18}^-$ that uncovered a 300 fs hole relaxation from HOMO -1 to HOMO. 48 The identical internal conversion time constants indicate that ligand substitution has minimal impact on internal conversion within core states.

The picosecond decay is attributed to intersystem crossing (ISC) to a high-spin complex mediated by Au-S vibrational modes, which was originally detected and assigned from nearinfrared transient absorption measurements.⁴⁸ Link and El-Sayed originally proposed an ISC channel for metal nanoclusters in order to reconcile visible transient absorption and emission data. 49 Recently, other researchers have also invoked this picosecond ISC process to explain transient spectroscopy data for Au₁₃ and biicosahedral Au₂₅ MPCs. ^{50,51} Furthermore, Au₂₅(PET)₁₈⁻ and short carbon chain aliphatic protected MPCs are efficient generators of singlet oxygen. 52,53 Later work found that long-lived triplet excited states exist in both aromatic and aliphatic ligand protected Au₂₅(SR)₁₈ and that this state is responsible for singlet oxygen generation.⁵³ Moreover, magnetic circular photoluminescence measurements on Au₂₅(PET)₁₈ confirmed that carriers relax into a distribution of emissive multiplet spin states uniquely coupled to vibrational modes.¹¹ In particular, the higher angular momentum state is strongly coupled to a Au-S vibrational mode. 11 As a result, the degree of nanocluster spin-polarized emission is influenced by the strength of electron-vibration coupling.⁵⁴ Based upon these data, the picosecond decay is assigned to intersystem crossing near the HOMO-LUMO energy gap that was mediated by Au-S vibrational modes.

Unreported, however, is the ligand dependence of the ISC relaxation channel. The aliphatic MPCs displayed accelerated ISC time constants compared to the aromatic MPC. Not only is intersystem crossing accelerated in the aliphatic series, it is more efficient. The branching ratio of the picosecond decay amplitude constant to the sum of all the amplitude coefficients reveals the preference of carrier relaxation to undergo ISC. The greater branching ratios for Au₂₅(SC6)₁₈⁻ and Au₂₅(SC12)₁₈⁻ compared to Au₂₅(PET)₁₈ indicate that intersystem crossing is a more prevalent relaxation pathway in the aliphatic MPCs. The long-lived decay component is attributed to a combination of radiative and nonradiative HOMO-LUMO carrier relaxation. After internal conversion, carriers can relax radiatively or nonradiatively into the ground state. In the aliphatic series, carriers have a greater propensity to undergo ISC and populate high-spin states.

The observed differences in the decay kinetics are attributed to ligand-dependent electron-vibrational coupling strength to the Au-S stretching mode. Cluster rigidity plays a major role

in electron-vibrational coupling and nonradiative decay rates. 33,55 Steric interactions, as well as the π interaction network, between the bulky aryl groups of the PET ligand can constrain the motion of the organometallic semiring. In contrast, the alkyl chain thiolate ligands have less steric interactions and hence primarily van der Waals forces contribute to the ligand-ligand interactions. Therefore, the semiring is likely less rigid for the aliphatic thiolate protected MPCs, and in turn, the rate of nonradiative decay coupled to semiring motion will increase. This interpretation is consistent with steady-state Raman spectra, which show a damped Au-S torsional signal for Au₂₅(SR)₁₈⁻ substituted with alkanethiols as compared to phenylethanethiol. 30,31 The decrease in semiring rigidity for aliphatic thiolate MPCs is further corroborated by photoluminescence measurements where the quantum yield decreases when substituting an aromatic ligand for an aliphatic ligand.⁵⁶ Greater electron-vibrational coupling lowers the quantum yield due to the greater contribution of nonradiative decay. In summary, the strength of electronic coupling to Au-S vibrations determines the efficiency of intersystem crossing in $Au_{25}(SR)_{18}^{-}$.

Rapid intersystem crossing is possible due to the high spinorbit coupling (SOC) of gold. SOC mixes excited singlet and triplet states. Further vibronic mixing can enhance ISC rates. Additionally, electronic states with higher angular momentum couple more strongly to vibrational modes in MPCs. For example, the radiative transitions of PdAu₂₄(PET)₁₈ have higher angular momenta and increased electron-vibrational coupling compared to the radiative transitions of Au₂₅(PET)₁₈. Therefore, it is reasonable that the triplet state would couple strongly to a Au–S vibrational mode. Given that core substitution can increase the angular momentum of excited states, metal doping may afford another avenue for tuning ISC rates. Both the metal and the passivating ligands should be considered for guiding carrier relaxation in MPCs.

Analysis of the high energy excited state absorption (ESA) kinetics gives further insight into the carrier relaxation mechanisms. The ESA peak at 2.10 eV was unique to $\mathrm{Au}_{25}(\mathrm{SC6})_{18}^-$ (blue line spectrum in Figure 1b). $\mathrm{Au}_{25}(\mathrm{PET})_{18}^-$ and $\mathrm{Au}_{25}(\mathrm{SC12})_{18}^-$ showed no comparable peaks. Both the PET- and SC12-substituted clusters showed nonzero ESA amplitude in this region, but only $\mathrm{Au}_{25}(\mathrm{SC6})_{18}^-$ showed a discrete peak. Figure S4 compares the evolution of the transient spectra with time. An ESA peak grows with increasing pump—probe time delay for $\mathrm{Au}_{25}(\mathrm{SC6})_{18}^-$. However, while the transient ESA amplitude does increase for $\mathrm{Au}_{25}(\mathrm{PET})_{18}^-$, a distinct peak does not develop. The kinetic trace extracted at 2.10 eV probe for $\mathrm{Au}_{25}(\mathrm{SC6})_{18}^-$ is shown in Figure 4. The fit is described by a 400 fs growth, a 2.5 ps decay and a long-lived decay.

Excited state absorption at higher probe energies can involve electronic states with ligand character. The signal buildup reflects hole relaxation to the HOMO. As carriers relaxed to the HOMO state (400 fs), a HOMO \leftarrow HOMO-n transition was observed. Based on theoretical predictions, the HOMO-n electronic state originates from the ligand band, which would explain why this ESA peak is unique to $\text{Au}_{25}(\text{SC6})_{18}^{-34}$ The transient signal decays as carriers undergo intersystem crossing (2.5 ps) and nonradiative decay (>ns) to the LUMO.

Based upon these results, a mechanism is shown in Figure 5. At 2.0 eV excitation, carriers are excited from the HOMO manifold to the LUMO manifold. Carriers relax through three competing pathways: (1) internal conversion, (2) intersystem

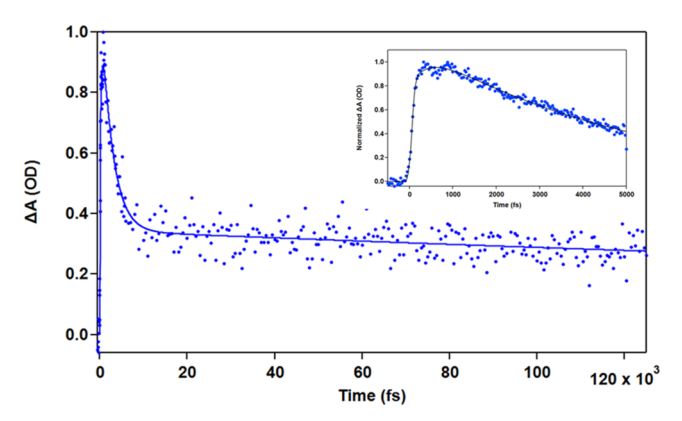


Figure 4. $\text{Au}_{25}(\text{SC6})_{18}^-$ kinetic trace acquired at 2.10 eV probe energy. The inset highlights the early time delay kinetics. The highenergy ESA kinetics resemble the low-energy ESA kinetics. There is a 400 fs growth, followed by a 2.5 ps decay and a long-lived decay. The 400 fs growth represents hole relaxation to the HOMO, where a HOMO \leftarrow HOMO-n spectroscopic transition develops as excited carriers populate the HOMO electronic state. The signal decays due to intersystem crossing (2.5 ps) and nonradiative relaxation on more persistent time scales.

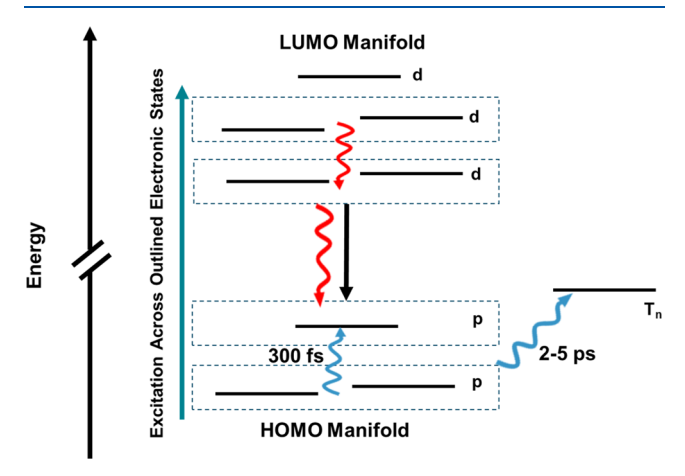


Figure 5. General mechanism for carrier relaxation in ${\rm Au_{25}(SR)_{18}}^{-}$ after intraband excitation. Broadband excitation centered at 2.0 eV is resonant with electronic transitions between the HOMO and LUMO manifold. The red (blue) arrows represent nonradiative electron (hole) relaxation.

crossing, and (3) radiative and nonradiative HOMO–LUMO relaxation. Carriers undergo rapid internal conversion through the HOMO (p) and LUMO (d) manifolds, mediated by Au–Au phonon modes. Hole relaxation from HOMO – 1 to HOMO occurs within 300 fs. Intersystem crossing to the triplet manifold (T_n) occurs within the HOMO manifold and is mediated by Au–S vibrational modes. The efficiency and rate of ISC are ligand dependent. Less rigid, aliphatic passivated MPCs display faster ISC rates and greater branching ratios compared to the more rigid aromatic thiolate MPCs.

CONCLUSIONS

The protecting ligand structure influences nonradiative relaxation rates and pathways in $Au_{25}(SR)_{18}^-$. A series of aliphatic $(Au_{25}(SC6)_{18}^-$, $Au_{25}(SC12)_{18}^-$) and aromatic $(Au_{25}(SR)_{18}^-)$ thiolate MPCs were studied using femtosecond time-resolved transient absorption spectroscopy. The transient signal amplitudes were modulated by 1.2 THz and 2.4 THz

oscillations from nanocluster quadrupolar core and breathing acoustic modes, respectively. The general agreement of the frequency, phase, amplitude, and dephasing time of the coherent oscillations suggested that the Au core was not distorted by the passivating ligands. The incoherent population decay displayed ligand-dependent dynamics on the picosecond time scale. In particular, intersystem crossing to high-spin states was accelerated and more efficient for nanoclusters protected with aliphatic thiolates than for aromatic thiolate protected MPCs. These results are attributed to aliphatic thiolate MPCs having a less rigid semiring due to weaker ligand-ligand interactions and reduced steric interactions as compared to aromatic thiolate protected MPCs. This semiring flexibility increased electron-vibrational coupling to staple unit vibrational modes and enhanced Au-S vibration mediated ISC. The results show that ligand design is a critical component for guiding ultrafast carrier relaxation dynamics in structurally precise gold nanoclusters. These energy relaxation processes are the primary determinants of many important applications, which include photocatalysis, singlet oxygen generation, and spin-polarized emission

ASSOCIATED CONTENT

Supporting Information

The Supporting Information is available free of charge at https://pubs.acs.org/doi/10.1021/acs.jpca.4c04387.

Additional coherent time-domain analysis and transient spectra (PDF)

AUTHOR INFORMATION

Corresponding Author

Kenneth L. Knappenberger, Jr. — Department of Chemistry, The Pennsylvania State University, University Park, Pennsylvania 16802, United States; oorcid.org/0000-0003-4123-3663; Email: klk260@psu.edu

Author

Nathanael L. Smith – Department of Chemistry, The Pennsylvania State University, University Park, Pennsylvania 16802, United States

Complete contact information is available at: https://pubs.acs.org/10.1021/acs.jpca.4c04387

Notes

The authors declare no competing financial interest.

ACKNOWLEDGMENTS

This work was supported by a grant from the Air Force Office of Scientific Research (FA9550-22-1-0402). Support by an award from the National Science Foundation (CHE-2204190) is also acknowledged

REFERENCES

- (1) Zhu, M.; Aikens, C. M.; Hollander, F. J.; Schatz, G. C.; Jin, R. Correlating the Crystal Structure of A Thiol-Protected Au25 Cluster and Optical Properties. *J. Am. Chem. Soc.* **2008**, *130*, 5832–6056.
- (2) Aikens, C. M. Electronic Structure of Ligand-Passivated Gold and Silver Nanoclusters. J. Phys. Chem. Lett. 2011, 2, 99–104.
- (3) Aikens, C. M. Origin of Discrete Optical Absorption Spectra of M 25(SH) 18- Nanoparticles (M = Au, Ag). *J. Phys. Chem. C* 2008, 112, 19797–19800.
- (4) Lopez-Acevedo, O.; Tsunoyama, H.; Tsukuda, T.; Häkkinen, H.; Aikens, C. M. Chirality and Electronic Structure of the Thiolate-

- Protected Au 38 Nanocluster. J. Am. Chem. Soc. 2010, 132, 8210–8218.
- (5) Li, G.; Abroshan, H.; Liu, C.; Zhuo, S.; Li, Z.; Xie, Y.; Kim, H. J.; Rosi, N. L.; Jin, R. Tailoring the Electronic and Catalytic Properties of Au25 Nanoclusters via Ligand Engineering. ACS Nano 2016, 10, 7998–8005.
- (6) Ramankutty, K. K.; Yang, H.; Baghdasaryan, A.; Teyssier, J.; Nicu, V. P.; Buergi, T. Molecule-like and Lattice Vibrations in Metal Clusters. *Phys. Chem. Chem. Phys.* **2022**, 24, 13848–13859.
- (7) Li, Y.; Jin, R. Magnetism of Atomically Precise Gold and Doped Nanoclusters: Delocalized Spin and Interparticle Coupling. *J. Phys. Chem. C* **2021**, *125*, 15773–15784.
- (8) Nealon, G. L.; Donnio, B.; Greget, R.; Kappler, J. P.; Terazzi, E.; Gallani, J. L. Magnetism in Gold Nanoparticles. *Nanoscale* **2012**, *4*, 5244–5258.
- (9) Chakraborty, I.; Pradeep, T. Atomically Precise Clusters of Noble Metals: Emerging Link between Atoms and Nanoparticles. *Chem. Rev.* **2017**, *117*, 8208–8271.
- (10) Rambukwella, M.; Sakthivel, N. A.; Delcamp, J. H.; Sementa, L.; Fortunelli, A.; Dass, A. Ligand Structure Determines Nanoparticles' Atomic Structure, Metal-Ligand Interface and Properties. *Front. Chem.* **2018**, *6*, No. 330.
- (11) Herbert, P. J.; Knappenberger, K. L. Spin-Polarized Photoluminescence in Au25(SC8H9)18 Monolayer-Protected Clusters. Small 2021, 17, No. 2004431.
- (12) Yi, C.; Zheng, H.; Herbert, P. J.; Chen, Y.; Jin, R.; Knappenberger, K. L. Ligand-and Solvent-Dependent Electronic Relaxation Dynamics of Au25(SR)18 Monolayer-Protected Clusters. *J. Phys. Chem. C* **2017**, 121, 24894–24902.
- (13) Yuan, X.; Goswami, N.; Mathews, I.; Yu, Y.; Xie, J. Enhancing Stability through Ligand-Shell Engineering: A Case Study with Au25(SR)18 Nanoclusters. *Nano Res.* **2015**, *8*, 3488–3495.
- (14) Wang, Y.; Bürgi, T. Ligand Exchange Reactions on Thiolate-Protected Gold Nanoclusters. *Nanoscale Adv.* **2021**, *3*, 2710–2727.
- (15) Chen, Y.; Liu, C.; Tang, Q.; Zeng, C.; Higaki, T.; Das, A.; Jiang, D. E.; Rosi, N. L.; Jin, R. Isomerism in Au28(SR)20 Nanocluster and Stable Structures. *J. Am. Chem. Soc.* **2016**, *138*, 1482–1485.
- (16) Häkkinen, H. The Gold-Sulfur Interface at the Nanoscale. *Nat. Chem.* **2012**, *4*, 443–455.
- (17) Qian, H.; Zhu, M.; Lanni, E.; Zhu, Y.; Bier, M. E.; Jin, R. Conversion of Polydisperse Au Nanoparticles into Monodisperse Au 25 Nanorods and Nanospheres. *J. Phys. Chem. C* **2009**, *113*, 17599–17603.
- (18) Li, J.-J.; Guan, Z.-J.; Lei, Z.; Hu, F.; Wang, Q.-M. Same Magic Number but Different Arrangement: Alkynyl Protected Au25 with D3 Symmetry. *Angew. Chem., Int. Ed.* **2019**, *123*, 13344–13353.
- (19) Shabaninezhad, M.; Abuhagr, A.; Sakthivel, N. A.; Kumara, C.; Dass, A.; Kwak, K.; Pyo, K.; Lee, D.; Ramakrishna, G. Ultrafast Electron Dynamics in Thiolate-Protected Plasmonic Gold Clusters: Size and Ligand Effect. *J. Phys. Chem. C* **2019**, *123*, 13344–13353.
- (20) Fei, W.; Antonello, S.; Dainese, T.; Dolmella, A.; Lahtinen, M.; Rissanen, K.; Venzo, A.; Maran, F. Metal Doping of Au25(SR)18-Clusters: Insights and Hindsights. *J. Am. Chem. Soc.* **2019**, *141*, 16033–16045.
- (21) Song, Y.; Zhong, J.; Yang, S.; Wang, S.; Cao, T.; Zhang, J.; Li, P.; Hu, D.; Pei, Y.; Zhu, M. Crystal Structure of Au25(SePh)18 Nanoclusters and Insights into Their Electronic, Optical and Catalytic Properties. *Nanoscale* **2014**, *6*, 13977–13985.
- (22) Gunawardene, P. N.; Corrigan, J. F.; Workentin, M. S. Golden Opportunity: A Clickable Azide-Functionalized [Au25(SR)18]-Nanocluster Platform for Interfacial Surface Modifications. *J. Am. Chem. Soc.* **2019**, *141*, 11781–11785.
- (23) Dainese, T.; Antonello, S.; Gascón, J. A.; Pan, F.; Perera, N. V.; Ruzzi, M.; Venzo, A.; Zoleo, A.; Rissanen, K.; Maran, F. Au25(SEt)-18, a Nearly Naked Thiolate-Protected Au25 Cluster: Structural Analysis by Single Crystal X-Ray Crystallography and Electron Nuclear Double Resonance. ACS Nano 2014, 8, 3904–3912.
- (24) Agrachev, M.; Antonello, S.; Dainese, T.; Gascón, J. A.; Pan, F.; Rissanen, K.; Ruzzi, M.; Venzo, A.; Zoleo, A.; Maran, F. A Magnetic

- Look into the Protecting Layer of Au25 Clusters. Chem. Sci. 2016, 7, 6910–6918.
- (25) De Nardi, M.; Antonello, S.; Jiang, D. E.; Pan, F.; Rissanen, K.; Ruzzi, M.; Venzo, A.; Zoleo, A.; Maran, F. Gold Nanowired: A Linear (Au25)n Polymer from Au 25 Molecular Clusters. *ACS Nano* **2014**, *8*, 8505–8512.
- (26) Green, T. D.; Yi, C.; Zeng, C.; Jin, R.; McGill, S.; Knappenberger, K. L. Temperature-Dependent Photoluminescence of Structurally-Precise Quantum-Confined Au25(SC8H9)18 and Au38(SC12H25)24 Metal Nanoparticles. *J. Phys. Chem. A* **2014**, *118*, 10611–10621.
- (27) Senanayake, R. D.; Akimov, A. V.; Aikens, C. M. Theoretical Investigation of Electron and Nuclear Dynamics in the [Au25(SH)-18]-1 Thiolate-Protected Gold Nanocluster. *J. Phys. Chem. C* **2017**, *121*, 10653–10662.
- (28) Devadas, M. S.; Bairu, S.; Qian, H.; Sinn, E.; Jin, R.; Ramakrishna, G. Temperature-Dependent Optical Absorption Properties of Monolayer-Protected Au25 and Au38 Clusters. *J. Phys. Chem. Lett.* **2011**, *2*, 2752–2758.
- (29) Nieto-Ortega, B.; Bürgi, T. Vibrational Properties of Thiolate-Protected Gold Nanoclusters. Acc. Chem. Res. 2018, 51, 2811–2819.
- (30) Varnholt, B.; Oulevey, P.; Luber, S.; Kumara, C.; Dass, A.; Bürgi, T. Structural Information on the Au-S Interface of Thiolate-Protected Gold Clusters: A Raman Spectroscopy Study. *J. Phys. Chem. C* **2014**, *118*, 9604–9611.
- (31) Varnholt, B.; Guberman-Pfeffer, M. J.; Oulevey, P.; Antonello, S.; Dainese, T.; Gascón, J. A.; Bürgi, T.; Maran, F. Vibrational Coupling Modulation in N-Alkanethiolate Protected Au25(SR)180 Clusters. *J. Phys. Chem. C* **2016**, *120*, 25378–25386.
- (32) Parker, J. F.; Weaver, J. E. F.; McCallum, F.; Fields-Zinna, C. A.; Murray, R. W. Synthesis of Monodisperse [Oct4N+][Au 25(SR)18-] Nanoparticles, with Some Mechanistic Observations. *Langmuir* **2010**, *26*, 13650–13654.
- (33) Heintzelman, D. J.; Nelson, S. A.; Knappenberger, K. L. Influence of Halogen-Solvent Hydrogen Bonding on Gold Nanocluster Photoluminescence. *J. Phys. Chem. Lett.* **2024**, *15*, 2951–2956.
- (34) Aikens, C. M. Geometric and Electronic Structure of Au25(SPhX) 18- (X = H, F, Cl, Br, CH3, and OCH 3). *J. Phys. Chem. Lett.* **2010**, *1*, 2594–2599.
- (35) Jiang, D. E.; Kühn, M.; Tang, Q.; Weigend, F. Superatomic Orbitals under Spin-Orbit Coupling. *J. Phys. Chem. Lett.* **2014**, *5*, 3286–3289.
- (36) Liu, Z.; Li, Y.; Kahng, E.; Xue, S.; Du, X.; Li, S.; Jin, R. Tailoring the Electron-Phonon Interaction in Au25(SR)-18Nanoclusters via Ligand Engineering and Insight into Luminescence. ACS Nano 2022, 16, 18448–18458.
- (37) Maioli, P.; Stoll, T.; Sauceda, H. E.; Valencia, I.; Demessence, A.; Bertorelle, F.; Crut, A.; Vallée, F.; Garzón, I. L.; Cerullo, G.; Del Fatti, N. Mechanical Vibrations of Atomically Defined Metal Clusters: From Nano- to Molecular-Size Oscillators. *Nano Lett.* **2018**, *18*, 6842–6849.
- (38) Jeffries, W. R.; Malola, S.; Tofanelli, M. A.; Ackerson, C. J.; Häkkinen, H.; Knappenberger, K. L. Coherent Vibrational Dynamics of Au144(SC8H9)60 Nanoclusters. *J. Phys. Chem. Lett.* **2023**, *14*, 6679–6685.
- (39) Crut, A.; Maioli, P.; Del Fatti, N.; Vallée, F. Anisotropy Effects on the Time-Resolved Spectroscopy of the Acoustic Vibrations of Nanoobjects. *Phys. Chem. Chem. Phys.* **2009**, *11*, 5882–5888.
- (40) Crut, A.; Maioli, P.; Del Fatti, N.; Vallée, F. Acoustic Vibrations of Metal Nano-Objects: Time-Domain Investigations. *Phys. Rep.* **2015**, *549*, 1–43.
- (41) Combe, N.; Saviot, L. Acoustic Modes in Metallic Nanoparticles: Atomistic versus Elasticity Modeling. *Phys. Rev. B* **2009**, *80*, No. 035411.
- (42) Martinet, Q.; Berthelot, A.; Girard, A.; Donoeva, B.; Comby-Zerbino, C.; Romeo, E.; Bertorelle, F.; van der Linden, M.; Van Der Linden, M.; Tarrat, N.; Combe, N. Performances of the Lamb Model to Describe the Vibrations of Gold Quantum-Sized Clusters. *J. Phys. Chem. C* 2020, *124*, 19324–19332.

- (43) Miller, S. A.; Womick, J. M.; Parker, J. F.; Murray, R. W.; Moran, A. M. Femtosecond Relaxation Dynamics of Au 25L 18-Monolayer-Protected Clusters. *J. Phys. Chem. C* **2009**, *113*, 9440–9444.
- (44) Sfeir, M. Y.; Qian, H.; Nobusada, K.; Jin, R. Ultrafast Relaxation Dynamics of Rod-Shaped 25-Atom Gold Nanoclusters. *J. Phys. Chem.* C 2011, 115, 6200–6207.
- (45) Zhou, M.; Tian, S.; Zeng, C.; Sfeir, M. Y.; Wu, Z.; Jin, R. Ultrafast Relaxation Dynamics of Au38(SC2H4Ph)24 Nanoclusters and Effects of Structural Isomerism. *J. Phys. Chem. C* **2017**, *121*, 10686–10693.
- (46) Kong, J.; Wu, Y. Z.; Zhou, M. Coherent Vibrational Dynamics of [Au25(SR)18]-Nanoclusters. *Chin. J. Chem. Phys.* **2021**, 34, 598–604.
- (47) Zhou, M.; Zeng, C.; Sfeir, M. Y.; Cotlet, M.; Iida, K.; Nobusada, K.; Jin, R. Evolution of Excited-State Dynamics in Periodic Au28, Au36, Au44, and Au52 Nanoclusters. *J. Phys. Chem. Lett.* **2017**, 8, 4023–4030.
- (48) Stoll, T.; Sgrò, E.; Jarrett, J. W.; Réhault, J.; Oriana, A.; Sala, L.; Branchi, F.; Cerullo, G.; Knappenberger, K. L. Superatom State-Resolved Dynamics of the Au25(SC8H9)18- Cluster from Two-Dimensional Electronic Spectroscopy. *J. Am. Chem. Soc.* **2016**, *138*, 1788–1791.
- (49) Link, S.; El-Sayed, M. A.; Schaaff, T. G.; Whetten, R. L. Transition from Nanoparticle to Molecular Behavior: A Femtosecond Transient Absorption Study of a Size-Selected 28 Atom Gold Cluster. *Chem. Phys. Lett.* **2002**, *356*, 240–246.
- (50) Yoshida, K.; Arima, D.; Mitsui, M. Dissecting the Triplet-State Properties and Intersystem Crossing Mechanism of the Ligand-Protected Au13 Superatom. *J. Phys. Chem. Lett.* **2023**, *14*, 10967–10973.
- (51) Mitsui, M.; Wada, Y.; Kishii, R.; Arima, D.; Niihori, Y. Evidence for Triplet-State-Dominated Luminescence in Biicosahedral Superatomic Molecular Au25 Clusters. *Nanoscale* **2022**, *14*, 7947–7979.
- (52) Kawasaki, H.; Kumar, S.; Li, G.; Zeng, C.; Kauffman, D. R.; Yoshimoto, J.; Iwasaki, Y.; Jin, R. Generation of Singlet Oxygen by Photoexcited Au25(SR) 18 Clusters. *Chem. Mater.* **2014**, *26*, 2777–2788.
- (53) Agrachev, M.; Fei, W.; Antonello, S.; Bonacchi, S.; Dainese, T.; Zoleo, A.; Ruzzi, M.; Maran, F. Understanding and Controlling the Efficiency of Au24M(SR)18 Nanoclusters as Singlet-Oxygen Photosensitizers. *Chem. Sci.* **2020**, *11*, 3427–3440.
- (54) Herbert, P. J.; Tofanelli, M. A.; Ackerson, C. J.; Knappenberger, K. L. The Influence of Pd-Atom Substitution on Au25(SC8H9)-18Cluster Photoluminescence. *J. Phys. Chem. C* **2021**, *125*, 7267–7275.
- (55) Pyo, K.; Thanthirige, V. D.; Kwak, K.; Pandurangan, P.; Ramakrishna, G.; Lee, D. Ultrabright Luminescence from Gold Nanoclusters: Rigidifying the Au(I)-Thiolate Shell. *J. Am. Chem. Soc.* **2015**, *137*, 8244–8250.
- (56) Wu, Z.; Jin, R. On the Ligand's Role in the Fluorescence of Gold Nanoclusters. *Nano Lett.* **2010**, *10*, 2568–2573.
- (57) Penfold, T. J.; Gindensperger, E.; Daniel, C.; Marian, C. M. Spin-Vibronic Mechanism for Intersystem Crossing. *Chem. Rev.* **2018**, *118*, 6975–7025.